Inferring Circulation and Lateral Eddy Fluxes in the Arctic Ocean's Deep Canada Basin Using an Inverse Method

HAYLEY V. DOSSER AND MARY-LOUISE TIMMERMANS

Yale University, New Haven, Connecticut

(Manuscript received 18 September 2017, in final form 28 November 2017)

ABSTRACT

The deep waters in the Canada Basin display a complex temperature and salinity structure, the evolution of which is poorly understood. The fundamental physical processes driving changes in these deep water masses are investigated using an inverse method based on tracer conservation combined with empirical orthogonal function analysis of repeat hydrographic measurements between 2003 and 2015. Changes in tracer fields in the deep Canada Basin are found to be dominated by along-isopycnal diffusion of water properties from the margins into the central basin, with advection by the large-scale Beaufort Gyre circulation as well as localized, vertical mixing playing important secondary roles. In the Barents Sea branch of the Atlantic Water layer, centered around 1200-m depth, diffusion is shown to be nearly twice as important as advection to lateral transport. Along-isopycnal diffusivity is estimated to be ~300–600 $m^2 s^{-1}$. Large-scale circulation patterns and lateral advective velocities associated with the anticyclonic Beaufort Gyre are inferred, with an average speed of 0.6 $cm s^{-1}$. Below about 1500 m, along-isopycnal diffusivity is estimated to be ~200–400 $m^2 s^{-1}$.

1. Introduction

Water properties in the Canada Basin, in the Arctic Ocean, are set by the temperature and salinity of the source waters and by the processes driving water mass evolution. In the deep Canada Basin, the circulation and mixing environment are poorly understood, with limited direct observations of dissipation and velocity. In this paper, we focus on the deep water masses found below roughly 700-m depth. Using yearly hydrographic profile data from 2003 to 2015, we investigate and quantify the processes driving changes in water mass properties using empirical orthogonal function (EOF) analysis and an inverse method based on the tracer conservation equations adapted for the deep Canada Basin.

Water masses in the Canada Basin are largely defined based on the origin of the inflow. Between roughly 200- and 2000-m depth, water of Atlantic origin enters the basin in a boundary current and a series of intrusive features. The Atlantic Water is divided into two branches: Fram Strait Branch Water (FSBW) and the deeper, cooler Barents Sea Branch Water (BSBW). BSBW is modified at the surface in the Barents Sea (Rudels et al. 2004) and found from roughly 700–2000-m depth in the Canada Basin.

The dominant circulation features affecting the Atlantic Water are thought to be a narrow, topographically steered boundary current and the wind-driven Beaufort Gyre. The boundary current transports Atlantic Water cyclonically around the basin, with inflow near the Northwind Ridge and Chukchi Borderland (e.g., see Woodgate et al. 2007). Spall (2013) used an idealized eddy-resolving numerical model to show that lateral eddy fluxes and vertical mixing in the basin interior are likely important factors in driving the cyclonic Atlantic Water boundary current circulation.

The anticyclonic Beaufort Gyre characterizes the central basin circulation (Newton and Coachman 1974; McLaughlin et al. 2009; Proshutinsky et al. 2009; McPhee 2013). Analyzing data between 1993 and 2007, McLaughlin et al. (2009) tracked a warm temperature anomaly in the FSBW as it spread across the Canada Basin and concluded that transport occurred through a combination of advection by the gyre and lateral spreading in intrusions [i.e., thermohaline features that were studied in detail by Walsh and Carmack (2002, 2003)]. Woodgate et al. (2007) used hydrographic data from a single expedition in 2002 to map anomalously warm FSBW and cool BSBW intrusions from the boundary current across the Chukchi Borderland to the Canada Basin.

Corresponding author: Hayley V. Dosser, hayley.dosser@yale.edu

DOI: 10.1175/JPO-D-17-0190.1

Below the BSBW lies a layer of relatively cool water, which forms a deep temperature minimum in the Canada Basin centered around roughly 2500-m depth (Timmermans et al. 2003, 2005; Carmack et al. 2012). The ~500–1000-m-thick deep temperature minimum layer (DTML) overlies the Canada Basin bottom water. The relatively cool water in the DTML likely enters the Canadian Basin from the Eurasian Basin (e.g., see Rudels et al. 2000), with the Canada Basin bottom waters likely being relic waters from previous dense water renewal hundreds of years ago (e.g., see Macdonald et al. 1993; Timmermans and Garrett 2006).

The bottom water layer is vertically homogeneous in both temperature and salinity and is kept well mixed by thermal convection driven by geothermal heat (Timmermans et al. 2003; Carmack et al. 2012). Analyzing hydrographic data from 1993, 1997, and yearly from 2002 to 2010, Carmack et al. (2012) observed the DTML and homogeneous bottom water warming at a constant rate of roughly 0.004°C decade^{-1}, which appears to be associated with a buildup of geothermal heat. The presence of a deep double-diffusive staircase at the base of the DTML suggests limited turbulent mixing of heat from the bottom water into the DTML, although there is evidence of enhanced turbulent mixing and density overturns on the slope (Timmermans et al. 2003).

Velocity measurements are rare in these deep waters, and the weak flow magnitudes are difficult to resolve. However, characterization of the flow field is possible through analysis of the temperature and salinity fields. The goal of the present analysis is to investigate changes in water mass properties and quantify lateral transport mechanisms in the deep Canada Basin from hydrographic data. We begin by using EOF analysis to determine spatial and temporal variations in the properties of the BSBW and DTML water masses and examine how properties vary with depth across the basin. We infer dominant mechanisms of lateral transport of water mass properties, which are further quantified by an inverse method.

The inverse method approach used is designed to determine the horizontal velocity field and along-isopycnal diffusivity that best explain observed changes in tracers—here, temperature and salinity—on isopycnal surfaces. Estimates are calculated from the best-fit solution to an overdetermined set of equations derived from the temperature and salinity conservation equations in advective–diffusive form. The velocity field is additionally constrained using a geostrophic streamfunction; however, the method does not require an assumed level of no motion (or level of known motion). The magnitude of the advective velocity is determined based on the temperature and salinity fields.

The inverse method is conceptually similar to those of Lee and Veronis (1991) and Zika et al. (2010), although the results of the inversion are limited to along-isopycnal diffusivity and velocity rather than three-dimensional fields. Unlike the beta spiral method (Stommel and Schott 1977) or the Bernoulli inverse method (Killworth 1986), the method is based on changes in a tracer field. To deal with the limitations inherent in the available data, and the small signals common to the quiescent deep Arctic, the method used is deliberately simplistic. It is designed to provide an order-of-magnitude estimate of the quantities of interest, which are then interpreted in combination with the results of the EOF analysis.

In section 2, we describe the repeat hydrographic survey data used in the analysis and the typical salinity and temperature structure observed in the deep Canada Basin. In section 3, we describe the inverse method and discuss the requirements for its implementation. Section 4 presents results from the EOF analysis that qualitatively and quantitatively describe water mass changes. Section 5 presents results from the inverse method and estimates of lateral advective velocity and diffusivity for each water mass. These results, in combination with the results of the EOF analysis, are discussed and summarized in section 6.

2. Data and water mass description

a. *Repeat hydrographic profiles*

Full-depth repeat hydrographic profiles were collected yearly in the Canada Basin during summer surveys of the Joint Ocean and Ice Studies (JOIS) and Beaufort Gyre Observing System (BGOS) programs; we use data from 2003 to 2015 (which are available online at http://www.whoi.edu/beaufortgyre/). Conductivity–temperature–depth (CTD) instrument resolution is ~0.0002 for salinity and 0.0003°C for temperature. CTD instrument accuracy is ±0.002 for salinity, ±0.001°C for temperature, and ±2 m for depth (see Carmack et al. 2012). We use 1-m vertically averaged data.

The typical hydrographic sampling pattern (Fig. 1a) provides approximately repeat spatial coverage. The Canada Basin is 3500–3800 m deep, with a slope in the southeast. A limited number of hydrographic profiles are available from the basin margins and the slope. The analysis is restricted to profiles in the deep Canada Basin, which we define as locations where the ocean bottom depth exceeds 3000 m, determined using the International Bathymetric Chart of the Arctic Ocean (IBCAO; Jakobsson et al. 2012). The influence of processes on the slope and near the basin margins is discussed in section 6.

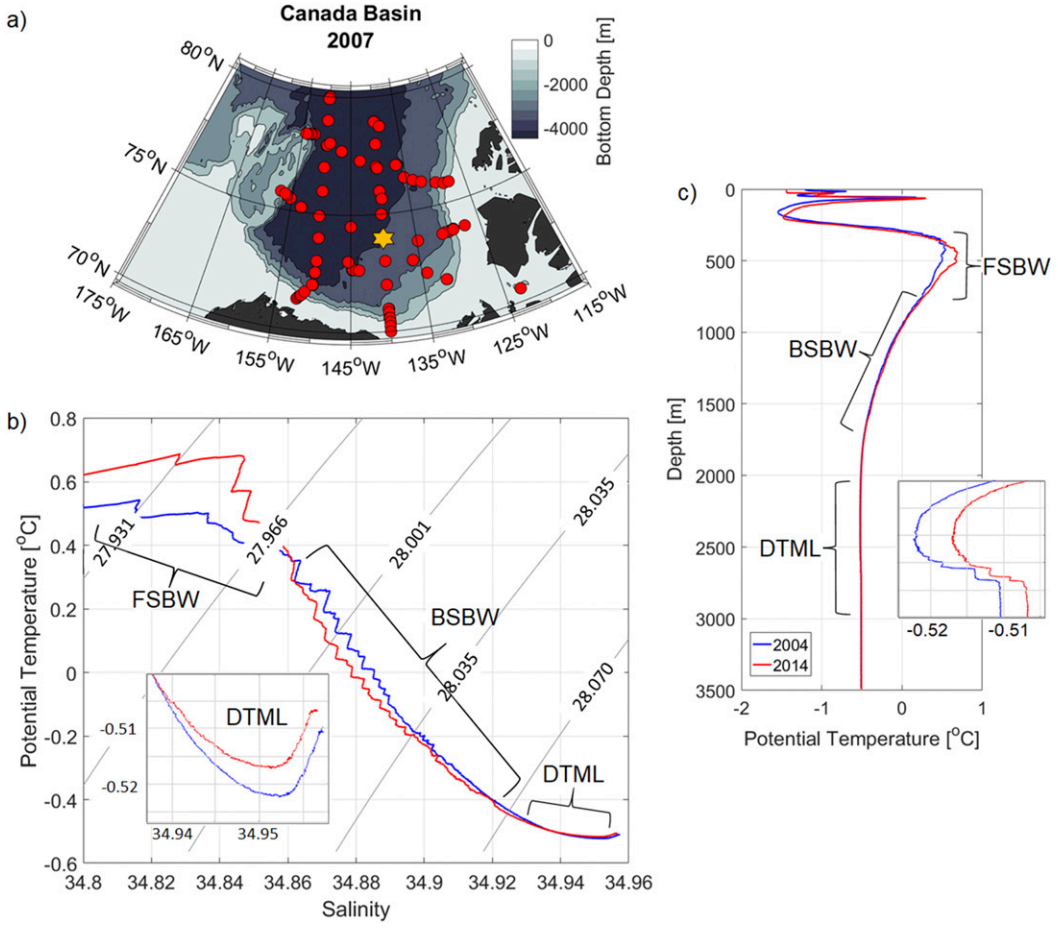

FIG. 1. (a) Map of Canada Basin showing typical hydrographic sampling pattern (from 2007). Contours show ocean bottom depth, with land in black. (b) Representative temperature–salinity diagram from 74°N, 140°W (gold star on map) from 2004 (blue) and 2014 (red), with isopycnals in gray. Water masses are labeled. Inset shows the DTML. (c) Profiles of potential temperature from the same location. Inset shows the DTML and deep double-diffusive staircase.

b. Water mass properties

Typical temperature and salinity profiles are shown in Figs. 1b and 1c. Below a shallow mixed layer and water of Pacific origin, two branches of the Atlantic Water enter the basin in a series of thermohaline intrusions, which are visible in a temperature–salinity (T–S) diagram as zigzags (Fig. 1b). Temperature and salinity increase with depth to the FSBW temperature maximum. Below the FSBW, smaller but more numerous intrusions carry cool BSBW from the boundary current into the deep basin. The thermohaline intrusions observed in the FSBW and BSBW spread laterally on near-isopycnal surfaces across Arctic basins (Carmack et al. 1998), exchanging properties through double-diffusive fluxes. The intrusions gradually change density as they spread as a result of vertical flux divergences, which are hypothesized to drive lateral fluxes (Carmack et al. 1998). Intrusions were first observed in the Canadian Basin in 1993 (Carmack et al. 1995) and had spread across the central Canada Basin by 2003 (McLaughlin et al. 2009). The DTML is characterized by a minimum in potential temperature at roughly 2500-m depth, below which presumed double-diffusive layers are evident (Timmermans et al. 2003; Fig. 1c, inset).

The analysis here focuses on the BSBW and DTML, but also includes the FSBW to enable comparison with a water mass for which the dynamics are better understood. Since the bottom water below the DTML is vertically and approximately laterally homogeneous (Carmack et al. 2012), it is not included in the analysis. We consider temperature and salinity variations along isopycnals [defined using potential density (σ) referenced to the surface]. As discussed in Zika et al. (2010), determining the magnitude of advection and diffusion of

tracers using an inverse method is best accomplished in an isopycnal reference frame. The use of potential density referenced to the surface as opposed to a deeper level does not significantly impact the results, either qualitatively or quantitatively. In particular, if a deep reference level (e.g., 1000 m) is used instead, the resulting estimates of diffusivity and velocity are well within the estimated uncertainty. The 28.097 kg m^{-3} isopycnal (potential density anomaly) is referred to as characteristic of the DTML, and the 28.010 kg m^{-3} and 27.925 kg m^{-3} isopycnals are referred to as characteristic of the BSBW and the FSBW, respectively.

We focus on potential temperature as the tracer of interest and note that temperature and salinity are interdependent but effectively passive tracers on isopycnals in the deep Canada Basin. A given temperature anomaly is density compensated by changes in salinity on an isopycnal, with salinity variations an order of magnitude smaller than temperature variations. Results are reported only for the potential temperature field; however, we find that they are qualitatively and quantitatively similar (to well within uncertainty) if salinity is used instead.

c. Time evolution

Observations indicate that the temperature of each of the three water masses of interest varies over the course of the record (Fig. 2). The FSBW in the central Canada Basin exhibits a general warming since 2003, the BSBW cooled at a constant rate over the course of the record from 2003 to 2015, while the DTML gradually warmed over the same time period.

The FSBW entering the Canada Basin in the early 2000s was characterized by anomalously warm maximum temperatures, >0.5°C up to 1°C, and increased salinity (McLaughlin et al. 2009). The warming trend in the FSBW in the Canada Basin began to level off in the mid-2000s, reflecting changes in the temperature of the boundary current inflow.

Between 2003 and 2015, the BSBW on $\sigma = 28.01\,\mathrm{kg\,m^{-3}}$ cooled by $-2.8 \times 10^{-3}\,^{\circ}\mathrm{C\,yr^{-1}}$ and freshened at a rate of $-1.9 \times 10^{-4}\,\mathrm{yr^{-1}}$, with similar rates of cooling and freshening at all stations within the deep basin. This change in water properties occurred at an approximately constant rate over the time period of interest. Woodgate et al. (2007) observed a cold anomaly in the BSBW in the Chukchi Borderland in 2002 with temperatures up to 0.5°C colder than the mean, associated with continual cooling and freshening of the inflow in the boundary current.

Between 2003 and 2015, the DTML on $\sigma = 28.097\,\mathrm{kg\,m^{-3}}$ warmed at a nearly constant rate of $3.5 \times 10^{-4}\,^{\circ}\mathrm{C\,yr^{-1}}$, with a linear increase in salinity of $2.2 \times 10^{-5}\,\mathrm{yr^{-1}}$; these

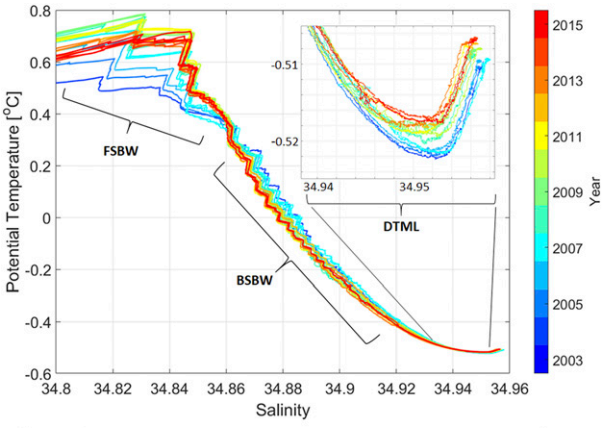

Linear trends in deep water mass properties		
	BSBW	DTML
	σ = 28.010 kg m^{-3}	σ = 28.097 kg m^{-3}
$\partial_t\theta$	-2.8 ± 0.3 x 10^{-3} °C yr^{-1}	3.5 ± 0.4 x 10^{-4} °C yr^{-1}
$\partial_t S$	-1.9 ± 0.2 x 10^{-4} yr^{-1}	2.2 ± 0.3 x 10^{-5} yr^{-1}

FIG. 2. Potential temperature θ, referenced to the surface, vs salinity S from 74°N, 140°W (gold star on map in Fig. 1), with profiles from 2003 to 2015 colored by year. Inset shows the DTML. Note that this general picture holds for all stations in the deep Canada Basin. Water masses are labeled, and the table below gives 2003 to 2015 trends in potential temperature $\partial_t\theta$ and salinity $\partial_t S$ on specified isopycnals in the BSBW and the DTML determined based on a linear fit to basin mean values for all profiles with ocean bottom depth >3000 m, with standard error.

trends are of the opposite sign and an order of magnitude smaller than the temperature and salinity trends characterizing the BSBW. Carmack et al. (2012) related warming of the DTML to geothermal heating; we additionally seek to address spatial variations in the temperature of the DTML, including lateral gradients and the presence of anomalously warm water near the basin margins and on the slope.

d. Spatial variations

Spatial patterns associated with the temperature of each water mass are presented qualitatively by objectively mapping all hydrographic profile data from 2003 to 2015, after first subtracting the isopycnal-mean potential temperature anomaly for each year (Fig. 3). Temperature variations are qualitatively different for each water mass, reflecting the inflow of cold BSBW in the boundary current, as opposed to warm anomalies for the FSBW and DTML.

The warmest FSBW is near the boundary current inflow at the northern part of the Northwind Ridge. McLaughlin et al. (2009) related warming of the FSBW in the north of the Canada Basin to northeastward advection by the anticyclonic Beaufort Gyre. The BSBW is coldest near the boundary current inflow, with a clear east–west temperature gradient [$O(10^{-7})$ °C m^{-1} on $\sigma = 28.01\,\mathrm{kg\,m^{-3}}$]. The DTML has a similar spatial

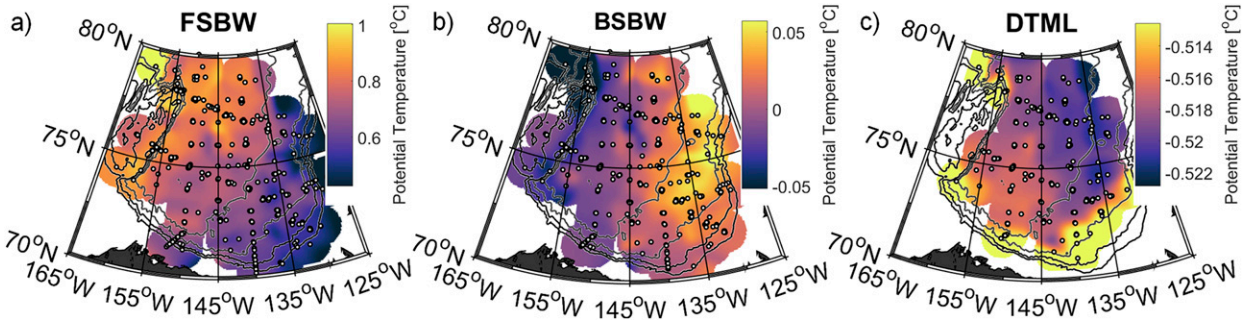

FIG. 3. Spatial maps of potential temperature referenced to the surface for the (a) FSBW on $\sigma = 27.925\,\mathrm{kg\,m^{-3}}$, (b) BSBW on $\sigma = 28.010\,\mathrm{kg\,m^{-3}}$, and (c) DTML on $\sigma = 28.097\,\mathrm{kg\,m^{-3}}$, objectively mapped using all hydrographic data from 2003 to 2015. The temporal trend about the mean has been removed before mapping. Regions farther than 100 km from a station location are masked out in white. Circles are station locations. Gray contours are the 500- to 3500-m isobaths in increments of 1000 m.

pattern to that of the BSBW in the deep basin but with the opposite sign gradient: warmer in the west and cooler in the east [$O(10^{-8})\,^{\circ}\mathrm{C\,m^{-1}}$ on $\sigma = 28.097\,\mathrm{kg\,m^{-3}}$]. The warmest water in the DTML is on the slope in the southeast and near the basin margins, rather than in the northern basin as for the FSBW. These spatial patterns are similar on all isopycnals within each water mass, and are quantified in section 4.

3. Inverse method theory

The inverse method originates from the tracer conservation equation in advective–diffusive form. Our goal is to determine large-scale lateral velocity and diffusivity estimates that best explain the observed tracer distribution. We make several simplifying assumptions, the validity of which are discussed further in the following sections.

We assume that across-isopycnal transport has a negligible effect on tracer properties relative to along-isopycnal transport. The presence and persistence of intrusions (Walsh and Carmack 2002, 2003) and double-diffusive staircases (Timmermans et al. 2003, 2008; Bebieva and Timmermans 2016) in the Canada Basin reflect low levels of mechanical mixing supported by observations (Rainville and Winsor 2008; Guthrie et al. 2013; Dosser and Rainville 2016). This assumption is likely inappropriate on the slope and near the margins of the basin, where the absence of a deep double-diffusive staircase suggests enhanced turbulent mixing (Timmermans et al. 2003).

Along-isopycnal eddy processes are parameterized in terms of a lateral diffusivity κ_H, following the standard Reynolds averaging approach, and this lateral diffusivity is assumed to be approximately constant on any isopycnal. This is likely a poor approximation, as it is known that eddy kinetic energy varies across the Canada Basin (Zhao et al. 2016), and as such the diffusivity should be treated as an approximate average on a given isopycnal.

There is no significant trend in the spacing between isopycnals in the deep water masses. Further, hydrographic profiles represent only a single snapshot of the basin stratification for each year. Therefore, divergence and convergence between isopycnals are not explicitly accounted for in the governing equations. The effect of eddy fluxes on along-isopycnal transport of the tracer is captured by the lateral diffusion term.

Applying the above assumptions to the advective–diffusive form of the potential temperature (θ) conservation equation, and assuming no sources or sinks in the deep basin, yields

$$\frac{\partial\theta}{\partial t} + u_g\frac{\partial\theta}{\partial x_\sigma} + v_g\frac{\partial\theta}{\partial y_\sigma} = \kappa_H\left(\frac{\partial^2\theta}{\partial x_\sigma^2} + \frac{\partial^2\theta}{\partial y_\sigma^2}\right),$$

where x_σ and y_σ are defined as the lateral, along-isopycnal coordinates, with z_σ as the normal, across-isopycnal coordinate. Hereinafter, we drop the σ on x, y, and z, and use subscripts for derivatives. Assuming that lateral circulation is predominantly geostrophic, the geostrophic velocity $\mathbf{u}_g = (u_g, v_g)$ may be written in terms of a streamfunction ψ as $u_g = -\partial_y\psi$ and $v_g = \partial_x\psi$. Here, these velocities represent flow along isopycnal surfaces:

$$\partial_t\theta - \partial_y\psi\partial_x\theta + \partial_x\psi\partial_y\theta = \kappa_H(\partial_{xx}\theta + \partial_{yy}\theta). \qquad (1)$$

The direction and magnitude of the velocity field are determined separately, which begins by writing the streamfunction in separable form: $\psi(x, y, z) = \Psi(z)\tilde{\psi}(x, y)$. Here, Ψ is a streamfunction amplitude determined from the inverse method (section 5a), and $\tilde{\psi}$ captures the spatially varying component of the streamfunction (i.e., defines the shape of streamfunction contours; section 4e).

Vertical velocity is assumed to be negligible for the gyre flow over the deep Canada Basin abyssal plain (where variations in the Coriolis parameter are negligible, i.e., an f plane); as a consequence, on a given horizontal surface, horizontal pressure gradients are everywhere parallel to horizontal density gradients (see, e.g., Hughes and Killworth 1995). Contours of constant density on a horizontal plane therefore have the same shape as geostrophic streamfunction contours $\tilde{\psi}$. Note that to estimate $\tilde{\psi}$ in isopycnal coordinates (section 4e), depth contours of a given isopycnal are used (equivalent to the use of isopycnal contours at a given depth level). Then $\mathbf{u}_g = \Psi(-\partial_y\tilde{\psi}, \partial_x\tilde{\psi}) = \Psi(\tilde{u}_g, \tilde{v}_g)$, and (1) becomes

$$\partial_t\theta + \Psi(\tilde{u}_g\partial_x\theta + \tilde{v}_g\partial_y\theta) = \kappa_H(\partial_{xx}\theta + \partial_{yy}\theta). \quad (2)$$

The streamfunction is normalized so that $|(\tilde{u}_g, \tilde{v}_g)|$ has unit mean. In this way, Ψ determines the magnitude of the velocity field, while $(\tilde{u}_g, \tilde{v}_g)$ set the direction of flow at each spatial location. We rearrange (2) as follows:

$$\frac{(\tilde{u}_g\partial_x\theta + \tilde{v}_g\partial_y\theta)}{\partial_t\theta} = \frac{\kappa_H}{\Psi}\frac{(\partial_{xx}\theta + \partial_{yy}\theta)}{\partial_t\theta} - \frac{1}{\Psi}, \quad (3)$$

such that κ_H/Ψ represents the slope of a line with intercept $-1/\Psi$. An analogous equation holds for salinity.

Equation (3) may be formulated to be independent of time, an approximation based on the observation that $\partial_t\theta$ and $\partial_t S$ are approximately constant over the course of the record in both the BSBW and DTML (section 2c). Further, similar values of $\partial_t\theta$ and $\partial_t S$ are found at all stations within the deep basin (ocean bottom depth >3000 m), which implies that spatial gradients do not change significantly between years. The accuracy of this approximation is examined in detail as part of the EOF analysis (section 4c). Equation (3) may then be expressed as

$$\tau_1(x, y) = \frac{\kappa_H}{\Psi}\tau_2(x, y) - \frac{1}{\Psi}, \quad (4)$$

where $\tau_1(x, y)$, estimated from observations, is an advective fraction representing changes in the temperature field associated with along-isopycnal advection, while $\tau_2(x, y)$ is a diffusive fraction representing variations associated with parameterized along-isopycnal diffusivity. Equation (4) has two unknowns, Ψ and κ_H, and is valid on any isopycnal in the BSBW or DTML water masses. A least squares linear fit to (4) yields Ψ and κ_H.

The streamfunction amplitude Ψ has units of diffusivity ($m^2 s^{-1}$), so that the dimensionless ratio κ_H/Ψ in (4) can be treated as a measure of the relative importance of along-isopycnal diffusion to advection in the evolution of the temperature (or salinity) field. For a diffusive–advective ratio greater than unity, lateral diffusion is the dominant driver of changes in water mass temperature and salinity, whereas advection dominates for $\kappa_H/\Psi < 1$. It is of interest to note that this ratio could be interpreted as an inverse Peclet number.

The calculation of spatial derivatives in (4) is nontrivial. Sparse data in some regions and scatter in the potential temperature field result in large uncertainties and discrepancies when calculating derivatives, and (4) requires second-order derivatives. Interpolating θ and S on an isopycnal using techniques such as objective mapping (Fig. 3) creates smoothly varying fields but are highly sensitive to outlying measurements, which may or may not be physical, increasing the uncertainty when taking derivatives. To more carefully quantify variations in properties in the deep water masses, we turn to EOF analysis.

4. Empirical orthogonal function analysis

Our goal in using EOF analysis is twofold: to quantify changes in water mass properties in the deep Canada Basin and to isolate the dominant spatial patterns in the potential temperature field in order to calculate large-scale, low-noise spatial derivatives for use with the inverse method.

a. Implementation

EOF analysis produces a set of ordered orthogonal modes, that is, the minimum number of independent patterns needed to capture the maximum amount of variance in the data. Spatial EOF modes are extracted for data sampled at different isopycnal levels (appendix) so that the principal components (PCs) show how the spatial modes vary between isopycnals (see, e.g., Gavart and De Mey 1997). Measurements of the form $A(x, y, z)$ are used, where A is a water property such as potential temperature or salinity. A separate EOF analysis is performed for each year and then the dominant modes for all years are compared.

The method is described by way of example (Fig. 4) with reference to potential temperature on isopycnals for a specific year (2004). Analysis is restricted to profiles in the deep basin, defined as locations with ocean bottom depths >3000 m. Isopycnals are chosen such that the average isopycnal depths are equally spaced between 300 and 3000 m, for 50 isopycnals from $\sigma = 27.8$ to 28.1 kg m^{-3}. EOF analysis identifies spatial patterns in temperature common to the FSBW, BSBW, and DTML water masses. Before the EOF analysis is performed, the potential temperature field on each isopycnal is normalized to have zero mean and unit standard deviation,

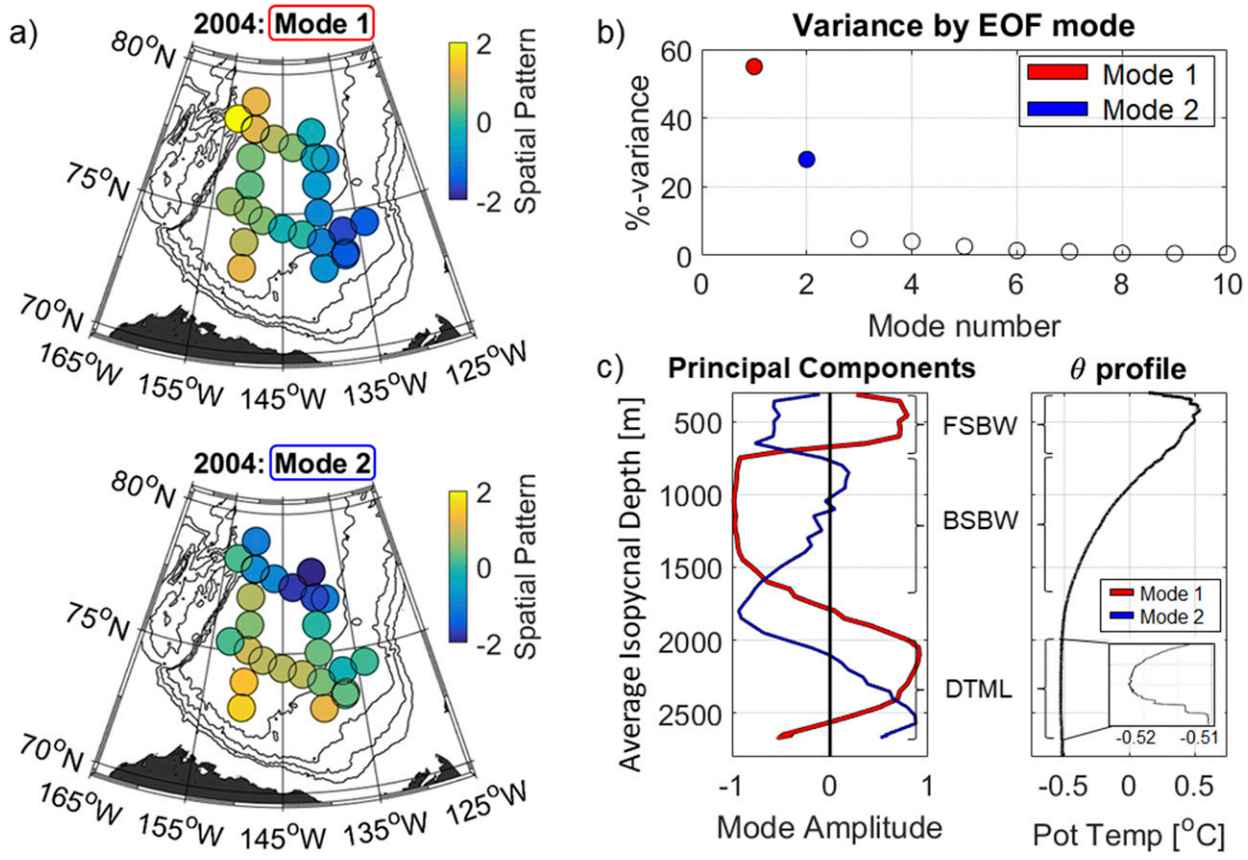

FIG. 4. (a) EOF mode-1 and mode-2 spatial patterns of potential temperature on isopycnals from 2004, normalized to unit standard deviation. Isopycnals are chosen to be spaced roughly every 50 m in the vertical in the FSBW, BSBW, and DTML water masses. (b) Total variance in the data explained by each EOF mode, cut off at the tenth mode. Only the first five modes are statistically distinguishable from noise. (c) Principal components corresponding to the first (red) and second (blue) EOF spatial modes, with normalized amplitudes that correspond to a one standard deviation change in the EOF modes, as in (a). The PCs are plotted as a function of average isopycnal depth, alongside a typical potential temperature profile with an inset showing the DTML. The approximate depth range for each water mass is indicated.

which ensures the results are not biased toward isopycnals with larger-amplitude temperature variations.

The first and second EOF modes for 2004, and the associated PCs, are shown in Figs. 4a and 4c. The sign of each mode on a given isopycnal is determined from the sign of the associated PC. The first EOF mode captures predominantly longitudinal variations in potential temperature (Fig. 4a) and captures 56% of the total variance in the normalized data (appendix; Fig. 4b), while the second mode has predominantly latitudinal variations and captures 25% of the total variance. The first and second modes together capture 81% of the variance in the normalized data. There is a clear separation between the variance explained by the first two modes and that explained by the third and higher modes (Fig. 4b). Modes higher than 5 are indistinguishable from noise.

The PCs provide the amplitude of each EOF mode on each isopycnal (Fig. 4c). The BSBW temperature field (~700–1500 m), for example, is well described by the first EOF mode alone (Fig. 4a, with opposite sign), consistent with qualitative observations of an east–west temperature gradient (Fig. 3b). The first EOF mode is also dominant within the DTML, while the first and second modes are important in the FSBW and near the base of the DTML in the double-diffusive staircase (Fig. 4c).

b. Interpretation of spatial modes

The spatial modes arising from the EOF analysis are statistical constructs assigned meaning based on existing knowledge of the system. While a single mode will never perfectly capture an underlying physical principle, they can provide insight into the physics governing a system. The first EOF mode (Fig. 4a) shows primarily a longitudinal gradient in temperature, consistent with warm (FSBW, DTML) or cold (BSBW) temperature

anomalies diffusing along isopycnals from the boundary current in the west into the deep basin. The fact that the first EOF mode is the dominant mode in the two deep water masses suggests that along-isopycnal diffusion may be the dominant process controlling changes in water mass properties, a hypothesis that will be explored further using the inverse method in section 5.

The second EOF mode shows a predominantly latitudinal temperature gradient and is of the opposite sign in the FSBW (warmer to the north) and the DTML (warmer to the south). In the FSBW, the second mode is likely associated with the anticyclonic Beaufort Gyre circulation. McLaughlin et al. (2009) linked advection by the gyre to warm temperature anomalies traveling from the boundary current across the northern basin. This interpretation is consistent with the stronger influence of the second mode on the FSBW relative to the BSBW (Fig. 4c), as the gyre is assumed to decrease in strength with depth. In the DTML, the second EOF mode is associated with anomalously warm temperatures in the southern basin, with possible sources near the margins and on the slope to the south. This is inconsistent with advection by an anticyclonic gyre but may be linked to enhanced mechanical mixing or cyclonic advection to be discussed further in sections 5 and 6.

c. *Similarity of EOF modes through time*

A separate EOF analysis is conducted for each year, and the resulting modes are compared. The EOF modes and PCs for a given year are calculated using potential temperature profiles from only that year. The isopycnals used are the same for all years, as is the restriction to profiles in the deep basin (bottom depth >3000 m). If the processes driving changes in water mass properties in the deep basin do not change significantly between years, we would expect similar EOF modes for all years.

From 2003 to 2015, the first EOF mode corresponding to each year explains between 45% and 70% of the total variance in the normalized potential temperature data for the FSBW, BSBW, and DTML water masses in the deep Canada Basin. The second mode explains 15% to 35% for a combined total of 70% to 85% variance explained by two modes alone. We conclude that the first two modes are sufficient to describe the water masses of interest for all years.

Spatial correlations quantify the similarity between the EOF modes from different years. To perform a correlation, the EOF mode is first mapped onto a 1° latitude by 4° longitude grid (Fig. 5b). If more than one data point falls within a grid box, the average value is used. To calculate the correlation coefficient r between any 2 years, only grid boxes with data available for both years are included. Because of the approximately repeat sampling pattern for the hydrographic stations, all years have most grid boxes in common.

The spatial patterns for the first EOF mode have high correlations between years, for all years from 2003 to 2015 (Fig. 5a), with $r \geq 0.75$. Therefore, the dominant feature of the potential temperature field in the deep Canada Basin over the last decade has been a persistent east–west gradient, despite temporal changes in the average temperature of each water mass. Correlation coefficients for the second EOF mode for all years range from $r = 0.55$ to $r = 0.95$ (not shown), suggesting that the dominant processes controlling variations in water mass properties do not change significantly during the 13 years considered.

d. *Structure in the vertical*

The principal components provide the amplitude of each EOF mode on each isopycnal. The mode amplitude is converted into percent variance explained by the first and second mode on each isopycnal for each year (appendix; Fig. 6). [This is equivalent to calculating variance by correlating the temperature field reconstructed from EOF mode 1 or 2 (appendix) with the observed potential temperature field.] For example, the PC associated with the first EOF mode in 2004 has an amplitude close to 1 in the BSBW (Fig. 4c) and explains nearly 100% of the variance in the BSBW potential temperature data (Fig. 6a, second column). The total variance explained by the first (or second) EOF mode is the average over all isopycnals for each year.

Potential temperature on isopycnals in the FSBW is described primarily by the second EOF mode (Fig. 6b) for all years except 2003 and 2004 when the first mode contributes significantly. After about 2004, the FSBW flowing into the Canada Basin no longer displayed the warming trend observed by McLaughlin et al. (2009; Fig. 2), which may account for the shift. The sign of the second mode is the same for all years (not shown), with warmer waters to the north.

For both the BSBW and DTML, the first EOF mode explains the majority of the temperature variance (usually 75% or higher) on most isopycnals, for all years (Fig. 6a), with spatial variations dominated by a basin-scale east–west gradient. The second EOF mode is intermittently important for a narrow range of isopycnals between the two water masses (centered slightly above 2000-m depth), where the sign of the temperature gradient reverses (cool vs warm anomaly) as well as in the deep double-diffusive staircase, where warmer waters are consistently found to the south of the basin. For isopycnals between the BSBW and DTML, variations in temperature are significantly smaller than for either water mass, and the second EOF mode likely has no

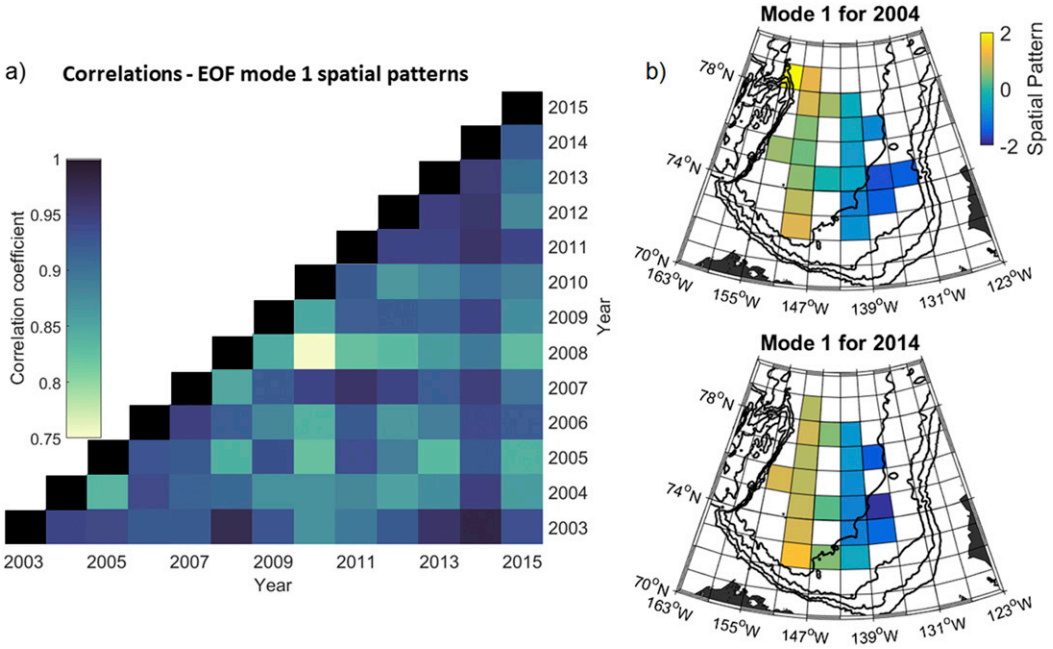

FIG. 5. (a) Correlation coefficients for the EOF mode-1 spatial pattern for each year with every other year for potential temperature on isopycnals. Note that the color scale begins at $r = 0.75$. (b) Spatial maps of the first EOF mode for 2004 and 2014 ($r = 0.95$), with the data averaged onto a 4° longitude by 1° latitude grid, which allows the correlations to be performed despite differences in precise station location from one year to the next. Only grid boxes with profile data available for both years are included in a given correlation.

consistent physical interpretation. Its interpretation in the deep staircase is discussed in section 6.

Both the first and second EOF modes are highly persistent between 2003 and 2015, with similar contributions to the temperature field on isopycnals throughout both the BSBW and DTML water masses. This indicates that along-isopycnal temperature gradients are qualitatively and quantitatively similar between years, which is consistent with the initial observation that the constant rate of cooling (BSBW) and warming (DTML) showed minimal variation between stations (Fig. 2; section 2c). The temporal coherence of the EOF modes

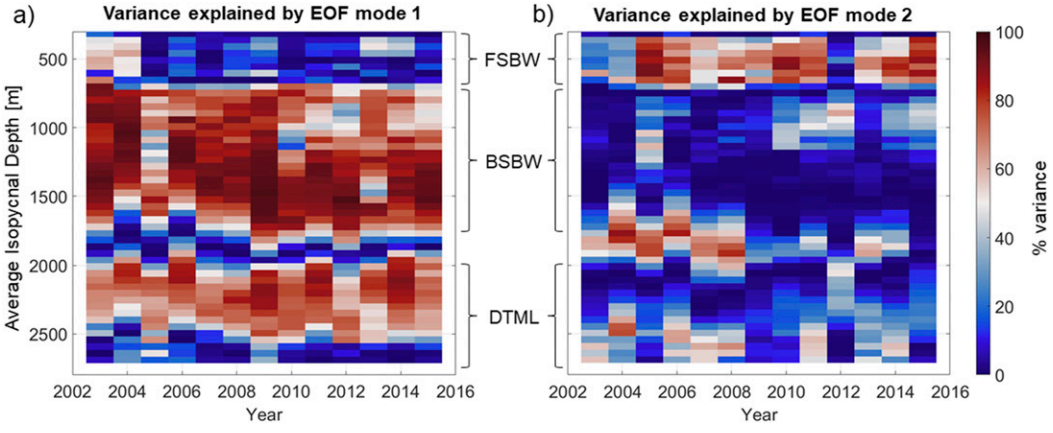

FIG. 6. (a) Percentage of the variance in the data on each isopycnal explained by the first EOF mode, for each year. The mode-1 spatial pattern for a given year captures a certain amount of the variability in the observed potential temperature field on each isopycnal, which is quantified by converting the first PC to percent variance explained (appendix). For example, the column for 2004 is calculated from the first PC for 2004 (Fig. 4c) and quantifies how well the first EOF mode for 2004 (Fig. 4a) captures variations in the observed potential temperature field from 2004. (b) As in (a), but for the second EOF mode.

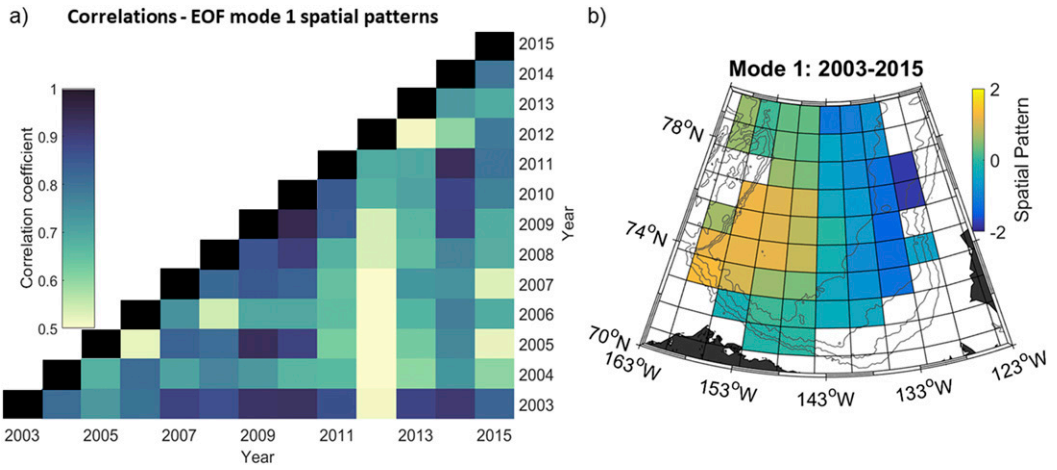

FIG. 7. (a) Correlation coefficients for correlations between the first EOF mode for isopycnal depth for each year from 2003 to 2015 with every other year. Note that the color scale begins at $r = 0.5$. To perform the correlations, data are gridded as in Fig. 5. (b) Grid average of the first EOF mode for isopycnal depth for every year from 2003 to 2015, for stations with bottom depth >3000 m. The spatial pattern has been scaled to have standard deviation equal to one. Higher (more positive) values correspond to isopycnal depths farther down in the water column. Light gray lines are the 500-, 1500-, 2500-, and 3500-m isobaths.

and associated PCs further suggests that the physical processes driving changes in water mass properties do not change between 2003 and 2015.

e. *Isopycnal depth and the streamfunction*

A similar EOF analysis to that for temperature is conducted for isopycnal depth to determine the geostrophic streamfunction contours, as defined in section 3. The magnitude of the geostrophic velocity field is determined from the inverse method, while the streamfunction contours on each isopycnal $\tilde{\psi}(x, y)$ are determined using depth contours of a given isopycnal.

An EOF analysis of the isopycnal depth field is performed for each year from 2003 to 2015. The first EOF mode (Fig. 7b) captures the majority of the variability in isopycnal depth for all years, explaining between 75% and 90% of the variance, with an average of 84%. The PC associated with the first EOF mode does not change sign with depth, that is, all isopycnals deepen toward the center of the Beaufort Gyre, forming a bowl shape centered near 74°N and 153°W. Unlike the EOFs for potential temperature, the second EOF mode for isopycnal depth explains less than 10% of the total variance on average and likely does not have a consistent physical interpretation.

Correlations between the first EOF mode for isopycnal depth for each year with every other year show reasonable similarity between years (Fig. 7a), with correlation coefficients of between 0.5 and 1.0. In 2012, isopycnals were flatter than during other years, perhaps reflecting observations that show an expansion of the Beaufort Gyre since 2007 (McPhee 2013). The mode-1 spatial patterns from 2003 to 2015 are appropriately normalized and grid averaged to produce a time-independent $\tilde{\psi}$ (Fig. 7b; sections 3 and 5a).

5. Inverse method results

The goal of the inverse method analysis is to estimate geostrophic velocity and along-isopycnal diffusivity on isopycnals within the BSBW and DTML water masses and relate these to circulation and transport of water mass properties.

a. *Inverse method implementation*

Spatial derivatives in (4) are calculated using a 2-mode reconstruction of the potential temperature field from the EOF analysis (appendix; Fig. 8), reintroducing dimensional units. When calculating the 2-mode reconstruction, the standard deviation of temperature on each isopycnal is reintroduced, but the mean is not, which effectively removes the temporal trend from the data.

The reconstructed fields are translated onto a 1° latitude by 4° longitude grid, as shown for $\tilde{\psi}$ in Fig. 7b. The size of a grid box is chosen to be consistent with the station spacing, with an associated length scale on the order of 100 km. Of course, the parameterized diffusivity κ_H is sensitive to the station spacing and length scale. The value of temperature within a grid box is the average of all data points within the grid box from all years. Since spatial gradients in temperature on an

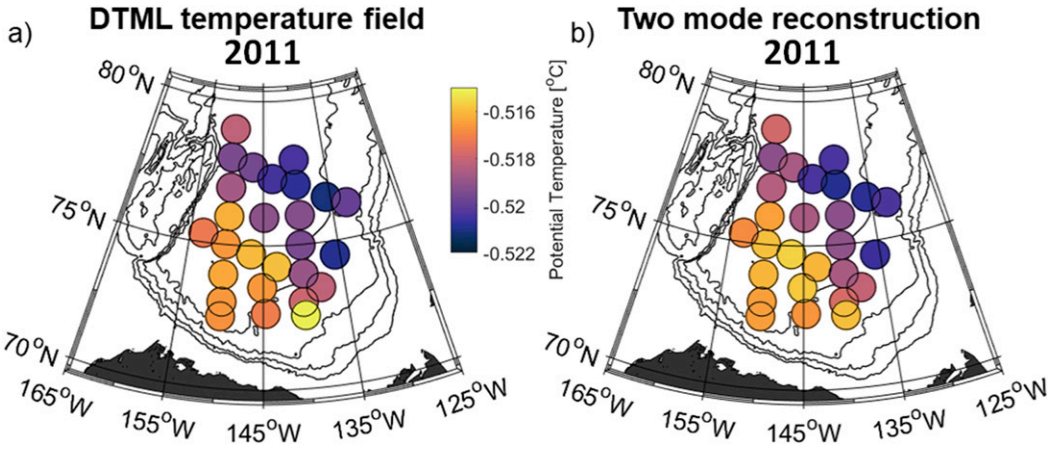

FIG. 8. (a) Potential temperature of the DTML on $\sigma = 28.097\,\mathrm{kg\,m^{-3}}$ in 2011. (b) Potential temperature field on the same isopycnal reconstructed using only the first two EOF modes. The color scale is the same for both fields, and the temporal trend has not been removed from the reconstructed field, to allow a one-to-one comparison. Black lines are the 500-, 1500-, 2500-, and 3500-m isobaths.

isopycnal vary negligibly in time between 2003 and 2015 (section 4), it is appropriate to combine data from all years to calculate derivatives (using centered finite differences), reducing uncertainty. Gridding the data and taking discrete derivatives imposes a length scale on the results but permits the calculation of first- and second-order spatial derivatives that reflect the observed, large-scale, slowly varying gradients in tracer fields.

Equation (4) is evaluated in each grid box on a given isopycnal; then, a least squares linear fit to τ_1 and τ_2 is used to determine the slope and intercept, from which Ψ, κ_H, and their uncertainties are calculated. The full geostrophic velocity field is then reconstructed from $u_g = -\Psi\partial_y\tilde{\psi}$, $\upsilon_g = \Psi\partial_x\tilde{\psi}$. Grid boxes are excluded when discrete spatial derivatives cannot be properly calculated because of the lack of data in adjacent grid boxes.

b. *Inverse method results for the BSBW*

We report results for isopycnals from $\sigma = 27.98\,\mathrm{kg\,m^{-3}}$ (with an average depth of ~700 m) to $\sigma = 28.06\,\mathrm{kg\,m^{-3}}$ (average depth ~1500 m) in the BSBW and use $\sigma = 28.01\,\mathrm{kg\,m^{-3}}$ as a representative example (Fig. 9). The inverse method least squares linear fit (Fig. 9a) has $r^2 = 0.5$. Out of 52 grid boxes containing data, 3 were discarded from the final fit because of the inability to calculate discrete derivatives. The slope gives a diffusive–advective ratio of $\kappa_H/\Psi = 2.0 \pm 0.3$. The intercept gives a streamfunction amplitude of $\Psi = 214 \pm 32\,\mathrm{m^2\,s^{-1}}$. Lateral diffusivity along the $\sigma = 28.01\,\mathrm{kg\,m^{-3}}$ isopycnal is then estimated to be $\kappa_H = 400 \pm 88\,\mathrm{m^2\,s^{-1}}$.

The average magnitude of the advective velocity field along $\sigma = 28.01\,\mathrm{kg\,m^{-3}}$ is $|\mathbf{u}_g| = 0.33 \pm 0.08\,\mathrm{cm\,s^{-1}}$. Flow speeds in individual grid boxes range from $|\mathbf{u}_g| = 0.05$ to $0.5\,\mathrm{cm\,s^{-1}}$. The full geostrophic velocity field on this isopycnal (Fig. 9b) is anticyclonic, with the isopycnal deepening to ~1000-m depth at the gyre center. Water appears to enter the basin moving eastward from the northern end of the Northwind Ridge.

Values for κ_H/Ψ for isopycnals within the BSBW range from 1.5 to 2.0, with an average value of 1.6 above about 1200 m, after which values decline with depth. Average velocity magnitudes on individual isopycnals within the BSBW range from $|\mathbf{u}_g| = 0.3$ to $1.2\,\mathrm{cm\,s^{-1}}$, with an overall average for the BSBW of $0.6\,\mathrm{cm\,s^{-1}}$. There is no significant trend in velocity magnitude with depth. Lateral diffusivity on isopycnals within the BSBW ranges from $\kappa_H = 205$ to $833\,\mathrm{m^2\,s^{-1}}$, with an average value of $462\,\mathrm{m^2\,s^{-1}}$.

The estimated values of the diffusive–advective ratio suggest that lateral diffusivity plays a dominant role in tracer transport in the BSBW above ~1200-m depth, being nearly twice as important to along-isopycnal variations in temperature and salinity as the geostrophic gyre circulation. This result is consistent with the EOF analysis results, where the first EOF mode—with primarily longitudinal variations consistent with eastward diffusion of anomalies transported by the boundary current along the western basin margin—explains most of the variance in the BSBW temperature and salinity fields (Fig. 6a). The second EOF mode, which is more likely associated with transport by the anticyclonic gyre, plays a secondary role in the BSBW (Fig. 9b).

In the deepest part of the BSBW (from ~1500–2000 m), the inverse method predicts cyclonic gyre circulation. This would suggest that the lateral pressure gradient at these

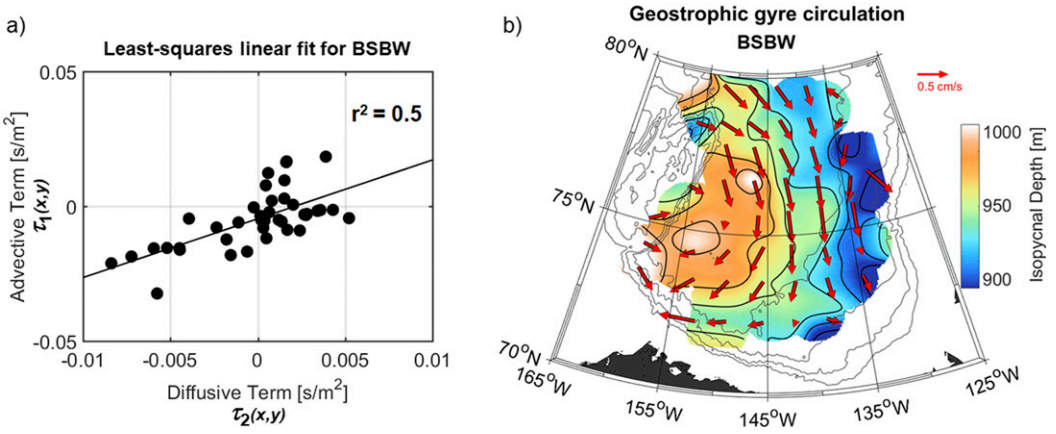

FIG. 9. (a) Least squares linear fit to data on $\sigma = 28.01\,\mathrm{kg\,m^{-3}}$ (BSBW) for the advective τ_1 and diffusive τ_2 terms in (4). Each point is the value from an individual grid box for the grid shown in Fig. 7. (b) Results for the estimated geostrophic Beaufort Gyre circulation on the same isopycnal, determined using the velocity magnitude calculated from the inverse method and velocity direction determined from the geostrophic streamfunction. Colors show the objectively mapped depth of the $\sigma = 28.01\,\mathrm{kg\,m^{-3}}$ isopycnal. Geostrophic flow is assumed to follow depth contours of a given isopycnal. Light gray lines are the 500-, 1500-, 2500-, and 3500-m isobaths.

depths has the opposite sign from that at shallower depths, such that the gradient is from low (in the gyre center) to high (at the periphery). This reversal of the gyre would also require that the geostrophic velocity pass through zero at some depth in the deep BSBW; inverse method results close to the transition are inherently uncertain and are not reported here.

c. *Results for the DTML*

In the DTML, the inverse method predicts cyclonic gyre circulation, so that Ψ is negative. We include isopycnals from $\sigma = 28.090\,\mathrm{kg\,m^{-3}}$ (with an average depth of ~2000 m) to $\sigma = 28.102\,\mathrm{kg\,m^{-3}}$ (average depth ~2800 m) in the DTML. Values for κ_H/Ψ are close to zero at the top and bottom of the DTML and within the double-diffusive staircase and range from −1.3 to −1.8 within the core of the water mass, with an average of −1.6. Average velocity magnitudes on isopycnals within the core of the DTML range from $|\mathbf{u}_g| = 0.2$ to $0.4\,\mathrm{cm\,s^{-1}}$, with an overall average of $0.3\,\mathrm{cm\,s^{-1}}$. Lateral diffusivity ranges from $\kappa_H = 198$ to $393\,\mathrm{m^2\,s^{-1}}$, with an average value of $305\,\mathrm{m^2\,s^{-1}}$, and then declines rapidly in the staircase. On $\sigma = 28.097\,\mathrm{kg\,m^{-3}}$, values are $\kappa_H/\Psi = -1.8 \pm 0.5$, $\kappa = 292 \pm 127\,\mathrm{m^2\,s^{-1}}$, and $|\mathbf{u}_g| = 0.2 \pm 0.1\,\mathrm{cm\,s^{-1}}$.

The diffusive–advective ratio in the DTML suggests that along-isopycnal diffusivity is more important than advection by the gyre to setting water mass properties. However, we note that it is possible that the presence of a warm θ anomaly in the southern deep basin causes the inverse method to incorrectly predict cyclonic gyre flow (in contrast to the FSBW, which had a warm anomaly in the north associated with anticyclonic transport by the gyre). Depending on the source of this warm anomaly, the assumptions used in the inverse method may not apply in the DTML, invalidating the results.

In particular, the assumption that vertical mixing is negligible may be inappropriate for the DTML. Timmermans et al. (2003) found evidence of enhanced turbulent mixing in the DTML on the slope in the southeast basin and noted that the deep double-diffusive staircase was eroded there. The staircase is also absent in the southwest in the deep basin (Fig. 10). Vertical mixing would warm the DTML, drawing (geothermal) heat and salt up from the homogeneous bottom layer below (Carmack et al. 2012), with the largest fluxes in the boundary regions. Note also that the highest temperatures are found along the presumed trajectory of the cyclonic boundary current (Fig. 10), suggesting advection by the boundary current may play a role.

Even if the prediction of cyclonic gyre flow is incorrect, results from the EOF analysis support the conclusion that along-isopycnal diffusion is the dominant mechanism transporting heat from the margins into the deep basin in the DTML. As in the BSBW, the first EOF mode explains the majority of the variance in the DTML above the deep double-diffusive staircase (Fig. 6). The second EOF mode in the DTML may be related to cyclonic gyre flow, turbulent vertical mixing, advection by the boundary current, or some combination thereof.

6. Summary and discussion

Using a novel inverse method based on tracer conservation in combination with EOF analysis of hydrographic

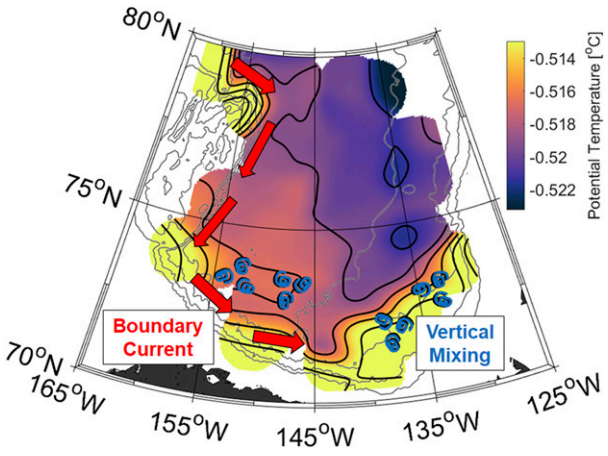

FIG. 10. DTML potential temperature on $\sigma = 28.097\,\mathrm{kg\,m^{-3}}$, objectively mapped as in Fig. 3, with black contours from −0.52° to −0.51°C in increments of 0.002°C, showing the roughly longitudinal variation across the central basin, and the influence of warming in the southern basin, near the margins, and on the slope. Red arrows show the assumed path of the boundary current, while blue spirals indicate regions with evidence of enhanced vertical mixing inferred from hydrographic profiles. Light gray lines are the 500-, 1500-, 2500-, and 3500-m isobaths.

data, we investigated the processes driving changes in water mass properties between 2003 and 2015 in the deep Canada Basin. Water mass transport was hypothesized to occur through a combination of advection by the large-scale Beaufort Gyre circulation and lateral diffusion of tracers from the basin margins. For both the BSBW and DTML deep water masses, along-isopycnal diffusivity appears to be the dominant process controlling changes in temperature and salinity in the deep basin, with relatively weak advection by the gyre. Both the gyre circulation and along-isopycnal diffusivity seem to be important in the FSBW, with the influence of the gyre dominating observed changes in tracer fields after 2004, as the rate of warming of the inflow tapered off.

Cooling and freshening was observed in the BSBW, while the DTML became warmer and saltier. In both deep water masses considered, EOF analysis was used to quantify changes in water mass properties. Potential temperature for a given isopycnal in these water masses changed at a steady rate through time from 2003 to 2015, with little variation between stations. Along-isopycnal temperature and salinity gradients were approximately constant between years and varied primarily from east to west in both the BSBW and the DTML, consistent with lateral diffusion. Smaller north–south gradients were linked to the Beaufort Gyre in the BSBW and to either the gyre or to vertical (geothermal) heat fluxes near the basin margins in the DTML.

In the BSBW, an approximate geostrophic velocity field consistent with the anticyclonic Beaufort Gyre circulation was determined by combining the results of the inverse method with a geostrophic streamfunction with ~100-km horizontal resolution. The overall average speed of along-isopycnal advection was $|\mathbf{u}_g| \sim 0.6\,\mathrm{cm\,s^{-1}}$. In the DTML, cyclonic circulation was predicted, with $|\mathbf{u}_g| \sim 0.3\,\mathrm{cm\,s^{-1}}$ on average. Beaufort Gyre current speeds below the FSBW in the central basin have previously been estimated to be $0–2\,\mathrm{cm\,s^{-1}}$, with large uncertainty (Newton and Coachman 1974). The center of the gyre was located near 74°N and 153°W, in reasonable agreement with recent results from Armitage et al. (2017), who observed the center of the Beaufort Gyre shifting northwest between 2003 and 2014, from ~74°N and 145°W to ~76°N and 150°W.

From the inverse method, lateral diffusivity is estimated to be $\kappa_H \sim 450 \pm 150\,\mathrm{m^2\,s^{-1}}$ in the BSBW and $\kappa_H \sim 300 \pm 150\,\mathrm{m^2\,s^{-1}}$ in the DTML, with an associated length scale of 100 km corresponding to the average grid spacing. We note that values of diffusivity from the inverse method are sensitive to this grid spacing length scale, which is itself determined by the hydrographic station spacing. Here, the lateral diffusivity accounts for any process that mixes potential temperature (or salinity) anomalies along isopycnals (contributions from, e.g., eddy fluxes and thermohaline intrusions). The contribution of along-isopycnal diffusion to the evolution of tracer fields is estimated to be up to twice as important as advection by the Beaufort Gyre circulation.

More direct estimates of eddy diffusivity (i.e., based on velocity fluctuations) are rare in the Arctic Ocean. For the oceans south of 60°N, Cole et al. (2015) estimated along-isopycnal diffusivities at 300-km scale using Argo profile data. Below ~1000-m depth, they found zonally averaged values of order $100–1000\,\mathrm{m^2\,s^{-1}}$. Employing a similar framework to Cole et al. (2015), Meneghello et al. (2018) estimate lateral diffusivities in the Canada Basin from velocity measurements to be $\sim 100\,\mathrm{m^2\,s^{-1}}$ on average at depths around 600 m, with an associated length scale of around 50 km. Near the basin margins and the Chukchi Plateau, Meneghello et al. (2018) found diffusivities elevated by a factor of 3 or more, associated with a more active eddy field.

The estimate of lateral diffusivity found here for the BSBW is significantly higher than previous estimates associated with thermohaline intrusions alone. Walsh and Carmack (2002, 2003) analyzed thermohaline intrusions in the Canada Basin FSBW and inferred lateral diffusivities in the range $50–200\,\mathrm{m^2\,s^{-1}}$. In the smaller-amplitude BSBW intrusions, κ_H is expected to be lower. This suggests that processes in addition to thermohaline

intrusion fluxes, such as stirring by eddies, are required to explain the value for lateral diffusivity in the BSBW.

The values inferred for κ_H may be used to estimate the approximate time required for a temperature anomaly to diffuse across the basin. A diffusivity of $\kappa_H = 400 \pm 88\,\mathrm{m^2\,s^{-1}}$ on $\sigma = 28.01\,\mathrm{kg\,m^{-3}}$ in the BSBW is associated with a rate of transport of 0.16–0.24 $\mathrm{cm\,s^{-1}}$, where κ_H is divided by the length scale associated with the centered difference used to calculate spatial gradients (200 km, twice the 100-km grid spacing length scale). At this rate, a temperature anomaly would be transported across the ~600-km-wide deep basin in 8–12 years. This is in rough agreement with the hydrographic observations, which show cold anomalies crossing the deep basin in about 10–12 years. McLaughlin et al. (2009) estimated a similar net rate of transport for the warm FSBW temperature anomaly of 0.1–0.5 $\mathrm{cm\,s^{-1}}$, which they associated with the combined effects of the gyre and thermohaline intrusions. In the DTML, values for diffusivity are lower than, but comparable to, those in the BSBW, in approximate agreement with hydrographic profile data that show warm anomalies crossing the deep basin in about 8–12 years.

We caution that the results of the inverse method in the DTML may be inaccurate because of the influence of enhanced vertical mixing in the southern basin near the margins and on the slope, transport by the poorly resolved cyclonic boundary current, or both. (The assumption that vertical mixing can be neglected in the BSBW appears valid.) Recall that the sign of the second EOF mode in the DTML is opposite that in the FSBW, reflecting a warm anomaly in the southern basin and resulting in the (potentially incorrect) prediction of cyclonic Beaufort Gyre flow. Although the exact heat budget of the DTML remains an open question, the available evidence from the EOF analysis and the inverse method both suggest that along-isopycnal diffusion of heat into the basin interior from the margins in the west and south is the most important factor.

While we have provided an alternate method of calculating lateral velocity and diffusivity, tighter constraints are needed on estimates of these quantities in the deep Canada Basin. Future studies might involve tracer release experiments, more extensive velocity measurements, or additional hydrographic data and mixing measurements (particularly near the basin margins), any of which would improve our understanding of the deep water masses. These deep water masses, which represent a significant fraction of the water column in the Canada Basin, provide a record of the evolution of the source waters and are an important component of the full Arctic Ocean heat and freshwater budgets.

Acknowledgments. The data were collected and made available by the Beaufort Gyre Exploration Program based at the Woods Hole Oceanographic Institution (http://www.whoi.edu/beaufortgyre) in collaboration with researchers from Fisheries and Oceans Canada at the Institute of Ocean Sciences. Funding was provided by the National Science Foundation Division of Polar Programs under Award Number 1350046.

APPENDIX

EOF Formalism

Potential temperature data are arranged into an $m \times n$ matrix $\mathbf{A}_\theta(\mathbf{x}, z)$ for n isopycnals sampled at m hydrographic stations, where $\mathbf{x} = (x, y)$. The mean potential temperature on each isopycnal $\mu_{\theta n}$ is subtracted from each data point on that isopycnal $A_{\theta n}$ (column means are removed), so that

$$\tilde{A}_{\theta n} = A_{\theta n} - \mu_{\theta n}.$$

To prevent the results from being biased toward spatial patterns in the FSBW, which has lateral variations an order of magnitude or more larger than those in the DTML, we divide the data on each isopycnal by the standard deviation of measurements on that isopycnal $\sigma_{\theta n}$ to give

$$X_{\theta n} = \tilde{A}_{\theta n}/\sigma_{\theta n}.$$

The result is a matrix $\mathbf{X}_\theta$ of potential temperatures on isopycnal surfaces spanning the FSBW, BSBW, and DTML, with zero mean and unit standard deviation.

EOF modes are determined using singular value decomposition, which produces ordered orthonormal modes, with the first mode capturing the most variance in the data. That is,

$$\mathbf{X}_\theta = \mathbf{USV}' = \mathrm{EOF}(\mathbf{x})\,\mathrm{PC}(z),$$

where the matrix $\mathbf{U}$ provides the spatial patterns for each EOF mode (the columns of $\mathbf{U}$ are the spatial EOFs), equivalent to the eigenvectors of the covariance matrix for $\mathbf{X}_\theta$. The diagonal elements of $\mathbf{S}$ provide the associated eigenvalues when squared and divided by the sample size. The columns of the matrix $\mathbf{V}$ provide the vertical structure of each EOF mode, and the principal components are calculated from PC = $\mathbf{SV}'$ (Fig. 4).

The principal components can be related to the variance explained by each EOF mode on each isopycnal as follows: $(\mathrm{PC}^M/\sqrt{m-1})^2$, where PC^M is the principal component for the Mth mode. This is equivalent to calculating the r^2 value for the correlation between that EOF mode's reconstructed temperature field and the potential temperature field on each isopycnal (Fig. 6).

To determine the sensitivity of the EOF results to spatial sampling and station locations, the data are subsampled by selecting random combinations of stations and correlating the resulting EOF modes to the original modes. Eliminating up to half of the original stations results in correlations above $r = 0.9$ for the first two modes, indicating very low sensitivity. EOF analysis is not affected by redundancy in the data; it does not require that measurements on successive isopycnals or between adjacent stations be independent.

EOF modes and the associated principal components are nondimensional and can be difficult to interpret in relation to the observations. The original data matrix is reconstructed as

$$\mathbf{A}_\theta(\mathbf{x}, z) = \mathbf{USV}'\sigma_\theta(z) + \mu_\theta(z),$$

where σ_θ and μ_θ are the standard deviation and mean of the potential temperature, respectively, on each isopycnal. A reconstruction of the potential temperature field can be accomplished using only a set number of modes. For example, a mode-1 reconstruction is given by

$$\mathbf{A}_\theta^{M1} = \mathbf{U}_{m1}\mathbf{S}_{11}\mathbf{V}'_{n1}\sigma_{\theta n} + \mu_{\theta n}.$$

The resulting $m \times n$ matrix provides the information in the original potential temperature field that is captured by the first EOF mode on each isopycnal at each station. As such, the reconstructed field has the same spatial pattern as the first EOF mode but provides dimensional values.

REFERENCES

Armitage, T. W. K., S. Bacon, A. L. Ridout, A. A. Petty, S. Wolbach, and M. Tsamados, 2017: Arctic Ocean surface geostrophic circulation 2003–2014. *Cryosphere*, **11**, 1767–1780, https://doi.org/10.5194/tc-11-1767-2017.

Bebieva, Y., and M.-L. Timmermans, 2016: An examination of double-diffusive processes in a mesoscale eddy in the Arctic Ocean. *J. Geophys. Res. Oceans*, **121**, 457–475, https://doi.org/10.1002/2015JC011105.

Carmack, E. C., R. W. Macdonald, R. G. Perkin, F. A. McLaughlin, and R. J. Pearson, 1995: Evidence for warming of Atlantic Water in the southern Canadian Basin of the Arctic Ocean: Results from the Larsen-93 expedition. *Geophys. Res. Lett.*, **22**, 1061–1064, https://doi.org/10.1029/95GL00808.

——, K. Aagaard, J. H. Swift, R. G. Perkin, F. A. McLaughlin, R. W. Macdonald, and E. P. Jones, 1998: Thermohaline transitions. *Physical Processes in Lakes and Oceans*, J. Imberger, Ed., Amer. Geophys. Union, 179–186.

——, W. J. Williams, S. L. Zimmermann, and F. A. McLaughlin, 2012: The Arctic Ocean warms from below. *Geophys. Res. Lett.*, **39**, L07604, https://doi.org/10.1029/2012GL050890.

Cole, S. T., C. Wortham, E. Kunze, and W. B. Owens, 2015: Eddy stirring and horizontal diffusivity from Argo float observations: Geographic and depth variability. *Geophys. Res. Lett.*, **42**, 3989–3997, https://doi.org/10.1002/2015GL063827.

Dosser, H. V., and L. Rainville, 2016: Dynamics of the changing near-inertial internal wave field in the Arctic Ocean. *J. Phys. Oceanogr.*, **46**, 395–415, https://doi.org/10.1175/JPO-D-15-0056.1.

Gavart, M., and P. De Mey, 1997: Isopycnal EOFs in the Azores Current region: A statistical tool for dynamical analysis and data assimilation. *J. Phys. Oceanogr.*, **27**, 2146–2157, https://doi.org/10.1175/1520-0485(0)027<2146:IEITAC>2.0.CO;2.

Guthrie, J. D., J. H. Morison, and I. Fer, 2013: Revisiting internal waves and mixing in the Arctic Ocean. *J. Geophys. Res. Oceans*, **118**, 3966–3977, https://doi.org/10.1002/jgrc.20294.

Hughes, C. W., and P. D. Killworth, 1995: Effects of bottom topography in the large-scale circulation of the Southern Ocean. *J. Phys. Oceanogr.*, **25**, 2485–2497, https://doi.org/10.1175/1520-0485(1995)025<2485:EOBTIT>2.0.CO;2.

Jakobsson, M., and Coauthors, 2012: The International Bathymetric Chart of the Arctic Ocean (IBCAO) version 3.0. *Geophys. Res. Lett.*, **39**, L12609, https://doi.org/10.1029/2012GL052219.

Killworth, P. D., 1986: A Bernoulli inverse method for determining the ocean circulation. *J. Phys. Oceanogr.*, **16**, 2031–2051, https://doi.org/10.1175/1520-0485(1986)016<2031:ABIMFD>2.0.CO;2.

Lee, J. H., and G. Veronis, 1991: On the difference between tracer and geostrophic velocities obtained from C-SALT data. *Deep-Sea Res.*, **38A**, 555–568, https://doi.org/10.1016/0198-0149(91)90063-L.

Macdonald, R., E. Carmack, and D. Wallace, 1993: Tritium and radiocarbon dating of Canada Basin deep waters. *Science*, **259**, 103–104, https://doi.org/10.1126/science.259.5091.103.

McLaughlin, F. A., E. C. Carmack, W. J. Williams, S. Zimmermann, K. Shimada, and M. Itoh, 2009: Joint effects of boundary currents and thermohaline intrusions on the warming of Atlantic Water in the Canada Basin, 1993–2007. *J. Geophys. Res.*, **114**, C00A12, https://doi.org/10.1029/2008JC005001.

McPhee, M. G., 2013: Intensification of geostrophic currents in the Canada Basin, Arctic Ocean. *J. Climate*, **26**, 3130–3138, https://doi.org/10.1175/JCLI-D-12-00289.1.

Meneghello, G., J. Marshall, S. Cole, and M.-L. Timmermans, 2018: Observational inferences of lateral eddy diffusivity in the halocine of the Beaufort Gyre. *Geophys. Res. Lett.*, **44**, 12 331–12 338, https://doi.org/10.1002/2017GL075126.

Newton, J. L., and L. K. Coachman, 1974: Atlantic Water circulation in the Canada Basin. *Arctic*, **27**, 297–303, https://doi.org/10.14430/arctic2886.

Proshutinsky, A., and Coauthors, 2009: Beaufort Gyre freshwater reservoir: State and variability from observations. *J. Geophys. Res.*, **114**, C00A10, doi:10.1029/2008JC005104.

Rainville, L., and P. Winsor, 2008: Mixing across the Arctic Ocean: Microstructure observations during the Beringia 2005 expedition. *Geophys. Res. Lett.*, **35**, L08606, https://doi.org/10.1029/2008GL033532.

Rudels, B., R. D. Muench, J. Gunn, U. Schauer, and H. J. Friedrich, 2000: Evolution of the Arctic Ocean boundary current north of the Siberian shelves. *J. Mar. Syst.*, **25**, 77–99, https://doi.org/10.1016/S0924-7963(00)00009-9.

——, E. P. Jones, U. Schauer, and P. Eriksson, 2004: Atlantic sources of the Arctic Ocean surface and halocline waters. *Polar Res.*, **23**, 181–208, https://doi.org/10.3402/polar.v23i2.6278.

Spall, M. A., 2013: On the circulation of Atlantic Water in the Arctic Ocean. *J. Phys. Oceanogr.*, **43**, 2352–2371, https://doi.org/10.1175/JPO-D-13-079.1.

Stommel, H., and F. Schott, 1977: The beta spiral and the determination of the absolute velocity field from hydrographic station data. *Deep-Sea Res.*, **24**, 325–329, https://doi.org/10.1016/0146-6291(77)93000-4.

Timmermans, M.-L., and C. Garrett, 2006: Evolution of the deep water in the Canadian Basin in the Arctic Ocean. *J. Phys. Oceanogr.*, **36**, 866–874, https://doi.org/10.1175/JPO2906.1.

——, ——, and E. Carmack, 2003: The thermohaline structure and evolution of the deep water in the Canada Basin, Arctic Ocean. *Deep-Sea Res. I*, **50**, 1305–1321, https://doi.org/10.1016/S0967-0637(03)00125-0.

——, P. Winsor, and J. A. Whitehead, 2005: Deep-water flow over the Lomonosov Ridge in the Arctic Ocean. *J. Phys. Oceanogr.*, **35**, 1489–1493, https://doi.org/10.1175/JPO2765.1.

——, J. Toole, R. Krishfield, and P. Winsor, 2008: Ice-tethered profiler observations of the double-diffusive staircase in the Canada Basin thermocline. *J. Geophys. Res.*, **113**, C00A02, https://doi.org/10.1029/2008JC004829.

Walsh, D., and E. Carmack, 2002: A note on evanescent behavior of Arctic thermohaline intrusions. *J. Mar. Res.*, **60**, 281–310, https://doi.org/10.1357/00222400260497499.

——, and ——, 2003: The nested structure of Arctic thermohaline intrusions. *Ocean Modell.*, **5**, 267–289, https://doi.org/10.1016/S1463-5003(02)00056-2.

Woodgate, R. A., K. Aagaard, J. H. Swift, W. M. Smethie, and K. K. Falkner, 2007: Atlantic Water circulation over the Mendeleev Ridge and Chukchi Borderland from thermohaline intrusions and water mass properties. *J. Geophys. Res.*, **112**, C02005, https://doi.org/10.1029/2005JC003416.

Zhao, M., M.-L. Timmermans, S. Cole, R. Krishfield, and J. Toole, 2016: Evolution of the eddy field in the Arctic Ocean's Canada Basin, 2005–2015. *Geophys. Res. Lett.*, **43**, 8106–8114, https://doi.org/10.1002/2016GL069671.

Zika, J. D., T. J. McDougall, and B. M. Sloyan, 2010: A tracer-contour inverse method for estimating ocean circulation and mixing. *J. Phys. Oceanogr.*, **40**, 26–47, https://doi.org/10.1175/2009JPO4208.1.